Structural, thermodynamic, and electronic properties of Laves-phase $NbMn_2$ from first principles, x-ray diffraction, and calorimetric experiments

X. Yan,[1,*] Xing-Qiu Chen,[1,†] H. Michor,[2] W. Wolf,[3] V. T. Witusiewicz,[4] E. Bauer,[2] R. Podloucky,[5] and P. Rogl[1]

[1]*Institute of Materials Chemistry, Vienna University, Währingerstrasse 42, 1090 Vienna, Austria*

[2]*Institute of Solid State Physics, Vienna University of Technology, Wiedner Hauptstrasse 8-10, 1040 Vienna, Austria*

[3]*Materials Design S.A.R.L., 44 avenue F.-A. Bartholdi, 72000 Le Mans, France*

[4]*ACCESS e. V., Intzestrasse 5, D-52072 Aachen, Germany*

[5]*Institute of Physical Chemistry, University of Vienna, Sensengasse 8, 1090 Vienna, Austria*

(Received 13 December 2017; revised manuscript received 21 February 2018; published 9 March 2018)

By combining theoretical density functional theory (DFT) and experimental studies, structural and magnetic phase stabilities and electronic structural, elastic, and vibrational properties of the Laves-phase compound $NbMn_2$ have been investigated for the C14, C15, and C36 crystal structures. At low temperatures C14 is the ground-state structure, with ferromagnetic and antiferromagnetic orderings being degenerate in energy. The degenerate spin configurations result in a rather large electronic density of states at Fermi energy for all magnetic cases, even for the spin-polarized DFT calculations. Based on the DFT-derived phonon dispersions and densities of states, temperature-dependent free energies were derived for the ferromagnetic and antiferromagnetic C14 phase, demonstrating that the spin-configuration degeneracy possibly exists up to finite temperatures. The heat of formation $\Delta_{298}H^0 = -45.05 \pm 3.64$ kJ (mol f.u. $NbMn_2$)$^{-1}$ was extracted from drop isoperibolic calorimetry in a Ni bath. The DFT-derived enthalpy of formation of $NbMn_2$ is in good agreement with the calorimetric measurements. Second-order elastic constants for $NbMn_2$ as well as for related compounds were calculated.

DOI: 10.1103/PhysRevB.97.125110

I. INTRODUCTION

Ground-state formation of electrons with magnetic degrees of freedom is an interesting and inexhaustible problem in solid-state physics. In simple cases, magnetic moments are expected to order below a defined temperature (Curie or Néel temperature). Geometrically frustrated magnets, however, represent an exception [1–4], where different spin configurations share the same energy. This gives rise to a large entropy at low temperatures or even at zero temperature, which seems to be in conflict with the third law of thermodynamics. The pyrochlore lattice is a typical example of such frustrated magnets. In these systems, pairwise spin interactions cannot be simultaneously minimized because of the lattice symmetry. The geometrical frustration can be so intense that it induces novel and complex phenomena [2] such as spin liquids [5], spin-orbit liquids [6], spin-ice states [3,4], spin clusters [4], and spin loops [7], as well as singlet formation [8].

So far, research on geometrically frustrated magnets has mostly focused on three classes of compounds of the same space group, $Fd\bar{3}m$: (1) $R_2T_2O_7$ (R = Y, Nd, Gd, Tb, Dy, Ho, Er, Yb; T = Ti, Mn, Mo, Ru, Cd, In, Sn, Tl), (2) AT_2O_4 or AT_2S_4 (A = Cd, Zn, Co, Mn, Ge, Mg, Cd; T = Ti, Cr, Fe, Ni, V, Cu), and (3) the cubic C15 structure of the itinerant-magnetic Laves phase, YMn_2 [9,10]. The R^{3+} ions in $R_2T_2O_7$, T^{2+} ions in AT_2O_4 or AT_2S_4, and Mn atoms in YMn_2 are magnetic, occupying the trigonal 16c (or 16d) sites which form a geometrically frustrated pyrochlore lattice. Neutron scattering and magnetic susceptibility measurements have demonstrated that these systems freeze into a disordered spin state at low temperatures and that the local nearest-neighbor spin correlations follow the two-in/two-out structure on vertices of each corner-sharing tetrahedra of the pyrochlore lattice. Although Y and Zr are neighbors in the periodic chart, YMn_2 behaves differently than $ZrMn_2$: $ZrMn_2$ exhibits a ferromagnetic ground state and has a very peculiar magnetically induced structural degeneracy (at least three structure types of C14, C15, and C36) at low temperatures from density functional theory (DFT) calculations [11,12], which have so far been unresolved by experiments [13]. Recent experiments [14] even demonstrated that a quantum criticality also exists in the C14 Laves-phase structure, $NbFe_2$. Because Nb is a neighbor of Zr in the periodic table, it is interesting to see which behavior will appear for the corresponding compound $NbMn_2$. Here, we use DFT calculations (like for $ZrMn_2$) to obtain the degenerate states between antiferromagnetic and ferromagnetic spin configurations with robust local moments of the spin systems in a geometrically frustrated C14 Laves-phase system, $NbMn_2$, at zero temperature. We find an interesting feature in which different spin configurations not only share the same DFT energy at the ground state but also result in almost the same densities of states at the Fermi level.

To date, only a few crystal structural experiments have been done [15,16] and have consistently showed that $NbMn_2$ crystallizes in the C14 Laves-phase structure.

*Present address: Institute of Solid State Physics, Vienna University of Technology, Wiedner Hauptstrasse 8-10, 1040 Vienna, Austria; yan@ifp.tuwien.ac.at

†xingqiu.chen@imr.ac.cn

The electronic structure and related physical properties of $NbMn_2$ still remain unclear, and no DFT calculation has been performed to date.

II. COMPUTATIONAL ASPECTS AND EXPERIMENTAL DETAILS

A. Computational aspects

To derive the density functional results the Vienna Ab initio Simulation Package (VASP) [17,18] with the projector augmented-wave potential [19,20] construction was applied. The potentials were constructed in such a way that semicore states (such as $3p$ states for Mn and corresponding s and p states of Nb) were treated as valence states. To approximate the exchange-correlation functional we made use of the generalized gradient approximation (GGA) of Ref. [21], including the approach of Vosko *et al.* [22] for spin-polarized calculations. Care was taken that total energies were converged in particular with respect to basis size and Brillouin zone integration. The energy cutoff for the plane-wave basis was chosen to be 400 eV. Full relaxation of geometrical parameters (atomic positions as well as all lattice parameters) was achieved by minimizing forces, stress tensor components, and total energies. For the derivation of local properties (such as projected densities of states and local magnetic moments) spheres with a radius of 1.556 Å were circumscribed at each atomic position.

The most abundant structural variants of the Laves phases are the C14, C15, and C36 structures. The C15 structure is fcc, belonging to the space group $Fd\bar{3}m$ O_h^7, No. 227. Both the hexagonal C14 and C36 structures belong to the space group $P6_3/mmc$ D_{6h}^4, No. 194. As a particular feature of all these structures we recognize planes forming triangular networks typical for a kagome lattice, clearly visible for the C14 and C36 structures in the [001] direction. It should be noted that such a network of vertex-sharing tetrahedra is a prime example of a geometrically frustrated system. For the C15 structure, such planes are of [111] orientation. For the C14 structure, two different Mn sites occur: the $2a$ site with higher coordination in the planes of triangles and the $6h$ site with lower coordination. For the C36 structure, three different Mn sites ($4f$, $6h$, and $6g$) are defined, whereas the high-symmetry C15 structure has only one crystallographic Mn site ($16d$).

In addition to non-spin-polarized (or nonmagnetic, NM) and ferromagnetic (FM) calculations some antiferromagnetic cases were studied. For the C14 structure three selected frequently observed antiferromagnetic initial spin arrangements were calculated (for the details of their magnetic ordering see Ref. [12]). We found the energetically stablest antiferromagnetic spin-up (+)/-down (−) arrangement (as also frequently observed in experiments): $2a(+)6h(++)2a(-)6h(---)$ along $\langle 0001\rangle$. The C15 antiferromagnetic structure was modeled according to Nakamura *et al.* [9], as proposed for YMn_2. For the C36 type, polymorph antiferromagnetic calculations were carried out in terms of the following initial spin arrangement: $6g(+++)4f(+)6h(++)4f(-)6g(---)4f(+)6h(---)4f(-)$ along $\langle 0001\rangle$.

The elastic constants for the C14 and C15 structures were derived from DFT total energies as a function of suitably selected distortions (see Refs. [23,24] for details). These energies were fitted to third-order polynomials, from which the elastic constants for the equilibrium structures were calculated. It should be noted that particularly for the C14 structure, a suitably large set of $\vec{k}$ points, $12 \times 12 \times 10$, has to be taken into account in order to get reliably converged results.

The phonon dispersions and phonon densities of states for the ferromagnetic and antiferromagnetic C14 structures were derived by making use of the so-called direct method [25] based on supercells with periodic boundary conditions [12]. The forces are computed for independent displacements required by the symmetry of the unit cell. A displacement amplitude of 0.03 Å was chosen. For the calculation of the force constants for both structures the corresponding supercells contain 36 atoms, and a $2 \times 2 \times 2$ $\vec{k}$-point grid was applied. Because the antiferromagnetic C14 phase has lower symmetry, it needs to run a total of 48 single-point energy calculations on supercells containing 36 atoms. However, for the ferromagnetic C14 case only 18 single-point energy calculations are necessary. All these calculations for deriving the force constants were again done using VASP.

B. Experimental details

All alloys (1 g each) were arc melted on a water-cooled Cu hearth from high-purity elements (more than 99.99 wt %) in Ti-gettered argon. A slight excess of Mn was used to compensate its evaporation during melting. Each alloy was weighed after melting, and Mn was added (if necessary) until the nominal composition was achieved. A part of each alloy was sealed in a vacuum quartz tube and annealed at 900 °C for 10 days prior to quenching into cold water.

Single crystals for single-crystal x-ray diffraction (SCXD) investigations were mechanically isolated from a crushed alloy, in which the composition was determined by electron probe microscopy analysis. For more details on the chemical analysis of our samples and structural analysis of our SCXD data, see Refs. [26,27].

For details about deriving the heat of formation of $NbMn_2$ via isoperibolic drop calorimetry see Sec. IV B and Ref. [28].

III. STRUCTURAL AND MAGNETIC STABILITIES

Figure 1 summarizes the calculated total energies as a function of volume per formula unit (f.u.) for C14, C15, and C36 structures in their NM, FM, and stablest antiferromagnetic (AF) states for $NbMn_2$. The right panel in Fig. 1 provides an overview of the total energies at equilibrium volumes of each phase, i.e., the minima of each energy-volume curve. In a first step, we focus our analysis on only nonmagnetic phases. Neglecting magnetism, the hexagonal C14 NM structure is found to be the stablest one. The C36 NM phase is less stable than the C14 NM phases by about 2 kJ mol^{-1}, whereas the C15 NM structure is less stable by about 3.8 kJ mol^{-1}. The predicted ground state is in agreement with the experimental observations of a stable C14 structure [15,16,29]. In a second step, the stable antiferromagnetic and ferromagnetic orderings are included in the DFT calculations. The phase stability sequence remains unchanged for nonmagnetic, antiferromagnetic, and ferromagnetic states. The experiments were typically performed at elevated temperatures (i.e., above

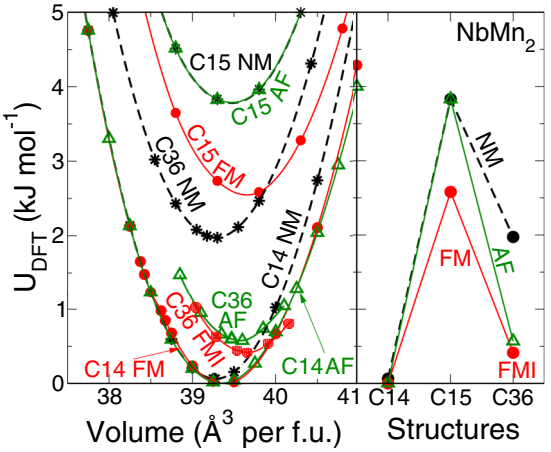

FIG. 1. Density functional total energy results for $NbMn_2$, Left: calculated total energies U_{DFT} as a function of volume V for the nonmagnetic case (NM; asterisks and solid lines) and the stablest antiferromagnetic (AF; triangles and dashed lines) and ferromagnetic (FM; solid circles and solid lines) spin ordering for C14, C15, and C36 structures. Each point corresponds to a structure obtained after relaxation of all structural parameters, resulting in the minimum of the total energy for a given fixed volume. Right: total energies U_{DFT} of all structures at the minima of the energy-volume curves in the left panel (i.e., at equilibrium volumes V_0). Energies refer to the lowest calculated energy of the C14 FM phase.

900 °C) on off-stoichiometric samples. No low-temperature crystal experiment on an exactly stoichiometric sample has been reported in the literature. This is mainly due to the difficulty in synthesizing a stoichiometric sample by directly arc melting two elements of quite different melting points (Nb: 2469 °C, Mn: 1246 °C). From the phase diagram [30], $NbMn_2$ was shown to congruently melt at 1500 °C at the stoichiometric composition with a C14 structure within a large-homogeneity region extending from ∼ 28 to ∼ 40 at % Nb. In contrast to this homogeneity range, the authors of Ref. [15] derived a rather restricted region within 31 to 36 at % Nb using a lattice parameter study at 900 °C as part of an investigation of the isothermal section Nb-Mn-Ga.

The C15 structure is stabilized (1.2 kJ mol^{-1}) only by ferromagnetism, and the antiferromagnetic ordering has no influence on the stability of the cubic C15 structure. The most striking feature is magnetic ordering of the hexagonal C14 and C36 structures, as illustrated in Fig. 1. For the C36 phase, the AF spin ordering is energetically more favorable by 1.4 kJ (mol f.u.) $^{-1}$ with respect to the NM phase, and the FM phase is even more stable by 0.2 kJ mol^{-1} as a result of the ferromagnetic and antiferromagnetic degeneracy. However, a truly unexpected result occurs for the C14 structure: FM and AF magnetic orderings possess the same ground-state total energies per f.u., and they are only slightly lower by 0.064 kJ mol^{-1} than for the non-spin-polarized NM ordering. This tiny energy difference is in line with rather small local magnetic moments, as discussed in Sec. V. Furthermore, the C14 AF and FM phases are energetically lower by only 0.4 kJ (mol f.u.)$^{-1}$ compared to those of C36 FM, which is another indication of degeneracies of (probably more complicated) magnetic orderings. These findings of degeneracy for $NbMn_2$ are in contrast to $ZrMn_2$, for which only the ferromagnetic states of C14, C15, and C36 are nearly degenerate because of the small difference of 0.3 kJ (mol f.u.)$^{-1}$, according to Refs. [11,12].

TABLE I. Calculated (calc.) and experimental (expt.) structural parameters with the C14, C15, and C36 crystal structures. Lattice parameters a and c are in Å, equilibrium volumes V_0 per formula unit are in Å ^{3}, and bulk moduli B are in GPa.

Structure	a	c	V_0	B	Method
C14 NM	4.799	7.874	39.28	248	calc.
C14 AF	4.802	7.881	39.38	219	calc.
C14 FM	4.803	7.887	39.40	220	calc.
$Nb_{36}Mn_{64}$	4.891	8.004	41.45		expt.[a]
$Nb_{30}Mn_{70}$	4.872	7.975	40.98		expt.[a]
	4.880	7.996	41.22		expt.[b]
	4.891	7.975	41.30		expt.[c]
	4.869	7.886	40.47		expt.[d]
C15 NM	6.817		39.30	250	calc.
C15 FM	6.846		39.50	206	calc.
C36 NM	4.804	15.730	39.33	249	calc.
C36 FM	4.820	15.773	39.66	196	calc.
C36 AF	4.815	15.778	39.60	221	calc.

[a]Reference [15].
[b]Reference [29].
[c]Reference [16].
[d]Reference .

For each structure and magnetic ordering, the equilibrium structural parameters are obtained from a full geometry optimization by minimizing the total energy. The results are listed in Table I, together with experimental data for the C14 structure [15,16,29]. The computed volume of the energetically most favorable C14 structure is smaller than the experimental data by 3%–4%. This discrepancy may, on the one hand, be attributed to the approximations made for exchange and correlation. On the other hand, the DFT calculations are representative for ideal stoichiometry at $T = 0$ K, whereas the experimental samples were fabricated at elevated temperatures for an extended range of homogeneity. Since ferromagnetic ordering tends to increase volumes [31], the nonmagnetic phases exhibit smaller lattice parameters and larger bulk moduli (e.g., by 20% for the C15 and C36 phases). However, for the C14 phase the equilibrium volumes of NM, FM, and AF are almost identical due to very small magnetic moments.

The refinement of our single-crystal data revealed isomorphism of the structure of $NbMn_2$ with the $MgZn_2$ type (C14 structure; see Table II). The heavier Nb is located at the 4f site, while Mn occupies the 2a and 6h sites. It is difficult to reveal possible defects since antisite atoms or vacancies at a level of about 5% can neither be determined from the refinement of the occupational numbers nor simply be judged from the atom displacement parameters. Nevertheless, the confidence level of the structure determination is very high ($R_F = 0.015$), and anisotropic thermal parameters of all atoms display almost spherical shapes, indicating a rather uniform bonding scheme. This is in line with interatomic distances, which merely reflect the sum of the atom radii (see Table II). The evaluated structural parameters are close to those in the literature [15,16,29].

TABLE II. Structure data derived from the refinement of the XSCD data (radiation: Mo $K\alpha, \lambda = 0.071069$ nm, $2^\circ < 2\theta < 72.45^\circ$) for $NbMn_2$ ($MgZn_2$ type, space group: $P6_3/mmc$).

Parameter	Value
Compound	$NbMn_2$
a, c (nm)	0.48917(2), 0.80030(4)
Reflections	1054
Number of variables	11
$R_F^2 = \sum \lvert F_o^2 - F_c^2 \rvert / \sum F_o^2$	0.015
ωR^2	0.036
R_{int}	0.064
GOF	1.149
Atomic parameters	
Nb in $4f(1/3,2/3,z),z$	0.56353(5)
Occ.	1.0(1)
$U_{11} = U_{22}; U_{33}$ 10^2(nm^2)	0.064(2); 0.062(2)
Mn1 at $6h(x,2x,1/4),x$	0.171186(3)
Occ.	1.0(1)
$U_{11}; U_{22}; U_{33}$ 10^2 (nm^2)	0.0062(2); 0.0056(3); 0.0060(2)
Mn2 at $2a(0,0,0)$, Occ.	1.0(1)
$U_{11} = U_{22}; U_{33}$ 10^2 (nm^2)	0.061(3); 0.065(4)
Interatomic distances (nm)[a]	
Nb-3Mn1	0.28607
Nb-3Mn1	0.28654
Nb-3Mn1	0.28655
Nb-3Mn2	0.28696
Nb-1Nb	0.29846
Nb-3Nb	0.30017
Mn1-2Mn1	0.23797
Mn1-2Mn2	0.24711
Mn1-2Mn1	0.25120
Mn1-2Nb	0.28607
Mn1-4Nb	0.28654
Mn2-6Mn1	0.24711
Mn2-6Nb	0.28696

[a]Standard deviation <0.0005 nm.

In compositions where Nb > 33.3 at %, besides the $4f$ site Nb also enters both the $2a$ and $6h$ sites of the structure, as shown in Fig. 2 for $Nb_{40}Mn_{60}$. In this compound the refined composition for the Laves phase is $Nb_{36.7}Mn_{63.3}$.

Comparing Tables III (DFT) and II (experiment) for the structural atomic parameters, one finds very good agreement for Nb at the $4f$ positions, whereas for Mn at the $6h$ position the experimental parameter is 0.01 larger than the DFT results. This difference might be related to the more complicated Mn-Mn interactions in the triangular sublattice and the approximations for exchange and correlation in the GGA functional. There is no significant difference in the parameters for the three different magnetic phases of the DFT calculations.

TABLE III. DFT-derived calculated internal parameters of atomic positions for the C14 structure of NM, FM, and AF phases of $NbMn_2$.

Wyckoff parameter	NM	FM	AF
Nb: $4f(1/3,2/3,z)$	0.5620	0.5629	0.5617
Mn: $6h(x,2x,1/4)$	0.1618	0.1616	0.1616
Mn: $2a(0,0,0)$			

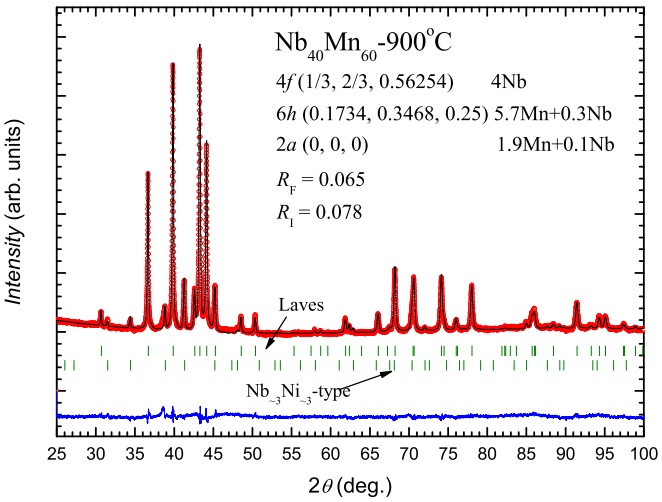

FIG. 2. Rietveld refinement of the XPD data for the alloy $Nb_{40}Mn_{60}$. The red circles are observations. The black line represents the model calculation. The vertical lines are Bragg positions for the $MgZn_2$-type Laves phase and the $Nb_{\sim 3}Ni_{\sim 3}$-type phase. The blue line is the difference between observations and calculations. The structural parameters and reliability factors are included.

IV. ENTHALPIES OF FORMATION FROM DFT CALCULATIONS AND CALORIMETRIC MEASUREMENTS

A. DFT calculation

The equilibrium enthalpies of formation ΔH for $NbMn_2$ can be calculated as the difference of density functional total energies U_{DFT} of the compound and its constituent elements, Nb and Mn, in their ground-state modifications,

$$\Delta H = U_{\text{DFT}}(\text{NbMn}_2) - [U_{\text{DFT}}(\text{Nb}) + 2U_{\text{DFT}}(\text{Mn})]. \quad (1)$$

The reference calculations for the bcc phase of Nb do not impose any technical issues; however, the ground state of solid Mn is extremely difficult to calculate because of the complicated noncollinear magnetic ordering of α Mn. For the derivation of this reference energy we made use of the high-temperature γ phase of Mn, for which DFT total energy calculations are feasible. Thus, a correction energy of 1.8 kJ mol^{-1} between the α Mn and the high-temperature γ phases was derived (for details see Ref. [12]). Then ΔH for $NbMn_2$ can be determined. Table IV presents the calculated ΔH for each structure for different magnetic orderings in their equilibrium state. The

TABLE IV. DFT-derived enthalpies of formation ΔH [kJ (mol f.u.)$^{-1}$] for nonmagnetic (NM), antiferromagnetic (AF), and ferromagnetic (FM) phases of $NbMn_2$.

	NM	AF	FM
C14	−46.496	−46.56	−46.56
Expt.[a]		-45.65 ± 3.64	
C15	−42.73	−42.73	−43.98
C36	−44.59	−45.94	−46.15

[a]Calorimetric data at 298 K in this work (see Sec. IV B).

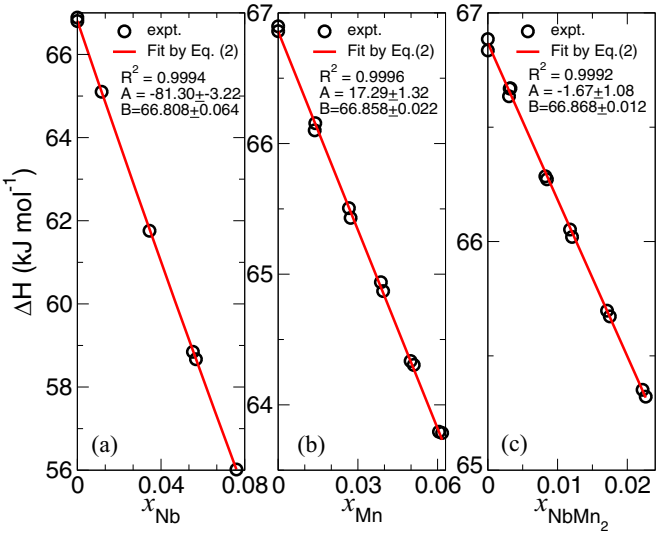

FIG. 3. Integral enthalpy of formation of (a) liquid binary Ni-Nb, (b) Ni-Mn, and (c) ternary Ni-Nb-Mn alloys due to the dropping of cold samples (298.15 K) of Nb, Mn, and $NbMn_2$ in a liquid-Ni bath at 1773 K.

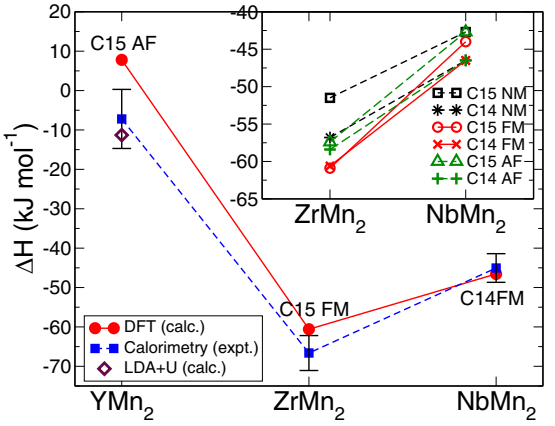

FIG. 4. DFT-derived enthalpies of formation for the stable ground state and calorimetric values at 298 K for YMn_2, $ZrMn_2$, and $NbMn_2$. For YMn_2 and $ZrMn_2$ DFT results refer to Refs. [12,34]; calorimetric data are taken from Refs. [13,34]. Inset: comparison of the structural competitions for the C15 and C14 phases depending on various spin polarizations for $ZrMn_2$ and $NbMn_2$.

ΔH differences between structures are very small, indicating close competition between the different phases.

B. Calorimetric measurements

The enthalpies of dissolution of pure Nb and Mn as well as of stoichiometric $NbMn_2$ in liquid Ni at 1773 ± 5 K were measured by drop isoperibolic calorimetry. Using these data, the integral enthalpies of formation of liquid binary Ni-Nb and Ni-Mn and ternary Ni-Nb-Mn alloys due to dropping of cold samples (298 K) were evaluated (for the details of the method see Ref. [28]). The results are shown in Fig. 3. It was found that the obtained integral values could be fitted properly using the following thermodynamically adapted power series [32]:

$$\Delta H = x(1-x)A + (1-x)B, \tag{2}$$

where A and B are fit parameters. The coefficient A denotes the molar enthalpy of dissolution of Nb, Mn, and $NbMn_2$ at infinite dilution $\Delta_{\text{diss}} H_i$, and B corresponds to the enthalpy change of 1 mol of pure Ni due to heating from 298 to 1773 K $\Delta H^{1773}_{298,\text{Ni}}$. The latter value can be compared with the one evaluated from the thermodynamic database for pure elements [33]. Table V summarizes the values obtained.

TABLE V. The partial enthalpy of dissolution of the pure substances and the $NbMn_2$ intermetallic in pure Ni at infinite dilution $\Delta_{\text{diss}} H_i$ at a temperature of 1773 ± 5 K.

Sample	$\Delta_{\text{diss}} H_i$ (kJ mol^{-1})	Error of $\Delta_{\text{diss}} H_i$ ($\pm 2\sigma$) (kJ mol^{-1})
Ni	66.84	0.05
	66.867 [a]	
Nb	−81.30	3.22
Mn	17.29	1.32
$NbMn_2$	−1.67	1.08

[a]Reference [33].

The standard enthalpy of formation of the intermetallic compound $NbMn_2$ referred to bcc Nb and bcc Mn at 298 K was evaluated using the values from Table V as follows:

$$\Delta_{298} H^0 = 2\Delta_{\text{diss}} H^0_{\text{Mn}} + \Delta_{\text{diss}} H^0_{\text{Nb}} - \Delta_{\text{diss}} H^0_{\text{NbMn}_2}. \tag{3}$$

The standard error (2σ) of the enthalpy of formation of the intermetallics was evaluated as

$$2\sigma = \sqrt{3.22^2 + 1.32^2 + 1.08^2}, \tag{4}$$

where 2σ denotes the error for $\Delta_{\text{diss}} H_i$. These calculations yielded

$$\Delta_{298} H^0 = -45.05 \pm 3.64\,\text{kJ(mol f.u. NbMn}_2)^{-1}. \tag{5}$$

In order to corroborate our calculated enthalpies of formation for $NbMn_2$ we consider all results of the related compounds XMn_2 (X = Y, Zr, Nb). In Fig. 4, the experimental and DFT enthalpies of formation are fairly consistent. The calorimetric data at 298 K for YMn_2 and $ZrMn_2$ are -6.0 ± 7.5 and -66.64 ± 4.44 kJ mol^{-1}, respectively [13]. Concerning the nonmagnetic phases, the C14 structure is clearly favored in all cases. However, by switching on spin polarization, antiferromagnetic ordering makes the C15 AF ground state more stable for YMn_2, with its energy lower by 8 kJ mol^{-1} than for the C14 AF phase (for details see Ref. [34]). For $ZrMn_2$, ferromagnetic ordering is favored: C15 FM is the stable structure, but C36 and C14 are less stable by only 0.2 and 0.3 kJ mol^{-1} in energy. For $NbMn_2$, the C14 crystal structure is lowest in enthalpy, and both ferromagnetic and antiferromagnetic orderings are degenerate. In addition, as seen in the inset of Fig. 4, the enthalpy differences for $NbMn_2$ are much smaller than for $ZrMn_2$, which is due to the much smaller local moments in $NbMn_2$, as discussed in Sec. V.

V. MAGNETIC PROPERTIES AND ELECTRONIC STRUCTURES FROM DFT CALCULATIONS

The magnetic moments and nearest-neighbor distances for antiferromagnetic and ferromagnetic C14, C15, and C36 structures of $NbMn_2$ are compiled in Table VI. For the C15 FM phase, because of cubic symmetry, there is only one Mn site ($16d$) with a local moment of $0.63\mu_B$ (the nearest-neighbor Mn-Mn distance is 2.4083 Å). For the hexagonal C14 and C36 structures, there are two and three different Mn sites, respectively, resulting in several distinctly different moments (Table VI).

Table VI reveals that for C14 AF and C14 FM the sizes of local Mn moments differ significantly. As shown in Fig. 5(a), Mn carries $0.64\mu_B$ and $0.35\mu_B$ at the $2a$ and $6h$ sites, respectively. The large moment of Mn at the $2a$ sites arises because of the Mn($2a$)-Mn($6h$) nearest-neighbor distance of 2.43 Å, which is slightly larger than the average Mn($6h$)-Mn distance of 2.41 Å. The shorter bond length quenches the moment at the $6h$ site because of increased hybridization. In the C14 AF structure, however, Mn($2a$) does not carry any moment, whereas Mn($6h$) possesses a local moment of $\pm 0.41\mu_B$, antiparallely coupled between two ($6h$) planes [Fig. 5(b)]. The most striking fact is that two different spin orderings, C14 AF and C14 FM, are not only energetically degenerate at 0 K but also possess almost the same atomic environments in terms of equilibrium volumes and nearly the same positional parameters (see Table III). In comparison with the neighboring isostructural compound $ZrMn_2$ [11,12], the C14 AF spin ordering is very different. For $ZrMn_2$ in the C14 AF structure only Mn($6h$) carries a large local moment of $\pm 1.35\mu_B$; no moment exists for Mn($2a$). Additionally, the magnetic moments of $NbMn_2$ are smaller than those of $ZrMn_2$ [12], mainly due to the smaller equilibrium volumes of $NbMn_2$ for all structures and magnetic orderings.

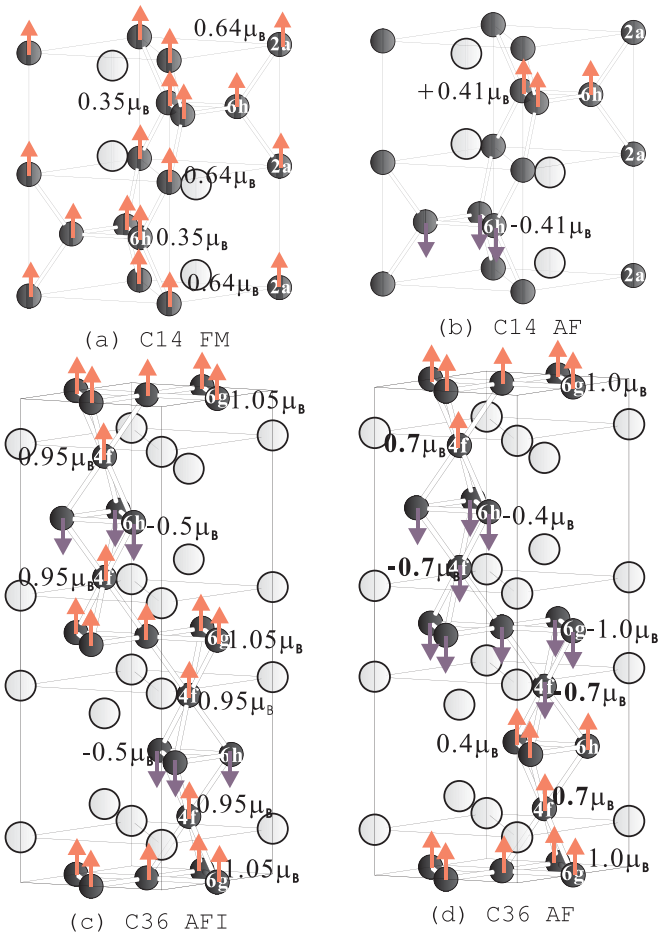

FIG. 5. Local magnetic moment arrangements of (a) FM and (b) AF ordering for two C14 structures and (c) AFI and (d) AF ordering of two C36 structures. Darker circles: Mn atoms; lighter circles: Nb atoms.

In comparison to the C14 structure, for C36 two different antiferromagnetic arrangements were stabilized after the self-consistent DFT calculations. Starting with the DFT calculation with ferromagnetic spin polarization, the C36 phase was converged to the antiferromagnetic ordering state [AFI; see Fig. 5(c)], for which three distinctly different Mn magnetic moments appear according to Table VI. The Mn($4f$) and Mn($6g$) sites couple parallel, carrying similar local moments of about $1.0\mu_B$. The Mn($6h$) sites, however, have a sizeable antiparallel moment of $-0.50\mu_B$ [Fig. 5(c)], resulting in a total moment of $1.78\mu_B$ per formula unit for the C36 AFI state. For C36 AF the magnetic ordering is more complex [Fig. 5(d)]. This phase is less stable than C36 AFI by about 0.2 kJ (mol f.u.)$^{-1}$. Magnetic ordering is invoked by Mn moments at the $6g$, $4f$, and $6h$ sites with an antiparallel orientation along the c axis, with sizes of $\pm 1.05\mu_B$, $\pm 0.7\mu_B$, and $\pm 0.40\mu_B$, respectively.

We also note the small induced moments of Nb [$0.02\mu_B$ antiparallel to Mn in C14 FM, $\pm 0.01\mu_B$ in C14 AF, $-0.06\mu_B$ for Nb($4f$) and $-0.03\mu_B$ for Nb($4g$) in C36 AFI, and $-0.05\mu_B$ for Nb($4g$) in C36 AF].

For $NbMn_2$, the C14 FM and AF phases are energetically rather close. Additionally, the stablest C14 FM phase is energetically more stable than the C36 AFI phase with a more complex magnetic ordering by only 0.4 kJ (mol f.u.)$^{-1}$. This clearly indicates the sensitivity of magnetic ordering to the local atomic environment of the Mn atoms. It might be suspected that noncollinear magnetic ordering is likely to occur because of the possible frustration of Mn magnetic moment orientations in the kagome lattice, which is typical for Laves-phase structures. Therefore, we cannot rule out more complicated spin configurations. However, due to the rather small magnetic moments we would not expect any substantial change in total energies and hence in the degeneracy of C14 FM and C14 AF.

The electronic band structures of C14 $NbMn_2$ are compiled in Fig. 6(a) for the nonmagnetic, ferromagnetic, and antiferromagnetic phases. In all cases the Fermi energy typically cuts through very flat bands along A $(0,0,\frac{2\pi}{a})$ to Γ (0,0,0) and to K $(\frac{2}{3}\frac{2\pi}{a},0,0)$. This results in high values of the DOS at the Fermi energy for all phases studied, as listed in Table VII. With and without spin polarizations, all the band structures of C14 are very similar, with only small shifts of spin-up and -down bands for the FM case. The shift is small because of the small magnetic moments. A very unusual feature is that for the magnetic C14 FM and C14 AF cases the DOS at E_F is high. The value for the total DOS at E_F of C14 NM remains almost unchanged compared with that of C14 FM. For the majority-spin component the value is lower by 15%,

TABLE VI. Magnetic properties of $NbMn_2$: local environment of Mn sites and distances d to nearest neighbors (nn) as well as averaged distance $\overline{d}$ (in Å). Calculated local magnetic moments are in units of μ_B, total magnetic moments are in units of μ_B per formula unit, and exchange splitting Δ is in eV for Mn d-like states for the C14, C15, and C36 ferromagnetic phases.

Ferro(i)magnetic						Antiferromagnetic					
Site	nn	d	$\overline{d}$	Magnetic moments	Δ	Site	nn	d	$\overline{d}$	Magnetic moments	Δ
C14 FM						C14 AF					
Mn(2a)	−6 Mn(6h)	2.4341	2.4341	0.64	0.62	Mn(2a)	−6 Mn(6h)	2.4334	2.4334	0.0	0.0
	−6 Nb(4f)	2.8168	2.8168				−6 Nb(4f)	2.8160	2.8160		
Mn(6h)	−2 Mn(2a)	2.4341	2.4123	0.35	0.33	Mn(6h)	−2 Mn(2a)	2.4334	2.4125	±0.41	±0.41
	−2 Mn(6h)	2.3308					−2 Mn(6h)	2.3315			
	−2 Mn(6h)	2.4718					−2 Mn(6h)	2.4726			
	−4 Nb(4f)	2.8112	2.8136				−4 Nb(4f)	2.8240	2.8557		
	−2 Nb(4f)	2.8186					−2 Nb(4f)	2.8016			
				0.84[a]						0.0[a]	
C15 FM											
Mn(16d)	−6 Mn(16d)	2.4082	2.4082	0.63	0.60						
	−6 Nb(8a)	2.8238	2.8238								
				1.20[a]							
C36 AFI						C36 AF					
Mn(4f)	−3 Mn(6g)	2.4519	2.4279	0.94	0.92	Mn(4f)	−3 Mn(6g)	2.4408	2.4266	±0.7	±0.68
	−3 Mn(6h)	2.4039					−3 Mn(6h)	2.4123			
	−3 Nb(4e)	2.8362	2.8264				−3 Nb(4e)	2.8306	2.8228		
	−3 Nb(4f)	2.8167					−3 Nb(4f)	2.8149			
Mn(6g)	−4 Mn(6g)	2.4098	2.4238	1.06	1.03	Mn(6g)	−4 Mn(6g)	2.4075	2.4186	±1.0	±0.99
	−2 Mn(4f)	2.4519					−2 Mn(4f)	2.4409			
	−4 Nb(4e)	2.8229	2.8227				−4 Nb(4e)	2.8224	2.8202		
	−2 Nb(4f)	2.8223					−2 Nb(4f)	2.8159			
Mn(6h)	−4 Mn(6h)	2.4967	2.4657	−0.45	−0.43	Mn(6h)	−4 Mn(6h)	2.4879	2.4627	±0.4	±0.38
	−2 Mn(4f)	2.4039					−2 Mn(4f)	2.4123			
	−4 Nb(4f)	2.8324	2.8260				−4 Nb(4f)	2.8346	2.8247		
	−2 Nb(4e)	2.8133					−2 Nb(4e)	2.8130			
				1.78[a]						0.0[a]	

[a]Total magnetic moment.

but the value of the minority component rises by about 20%. The total DOS at E_F for C14 AF gets even larger than that of C14 NM, by 20% (Table VII). This behavior is significantly different from $ZrMn_2$ [12], for which the total density of states at E_F is distinctly reduced by spin polarization. The occurrence of a high density of states at the Fermi level even for the spin-polarized calculations might be a hint of unusual electronic interactions.

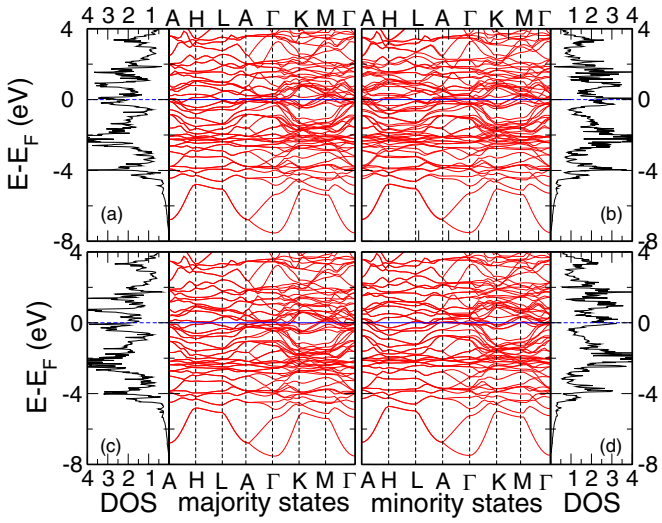

FIG. 6. Electronic valence band structure and density of states of C14 $NbMn_2$. (a) C14 NM, (b) C14 AF, (c) majority states of C14 FM, and (d) minority states of C14 FM.

For the C36 AF and AFI phases spin polarizations also lead to almost the same DOS at E_F. In contrast to the C14 cases, for C36 their spin-polarized densities of states are reduced by 20% with respect to the C36 NM phase. This difference might be attributed to the larger local magnetic moments for the C36 phases, resulting in a larger energy difference between spin-polarized C36 phases and C36 NM (see Fig. 1).

Table VII also lists the bare-band values of the Sommerfeld coefficient of the specific heat for a variety of calculated phases.

TABLE VII. DFT-derived total density of states at the Fermi level $N(E_F)$ (states eV^{-1} f.u.$^{-1}$) and specific-heat coefficients γ (mJ mol^{-1} K^{-2}) for the C14 and C36 phases of $NbMn_2$.

	C14 NM	C14 FM	C14 AF	C36 NM	C36 AFI	C36 AF
$N_\uparrow(E_F)$	2.22	1.82	2.49	2.84	1.99	2.07
$N_\downarrow(E_F)$	2.22	2.70	2.49	2.84	2.29	2.07
$N_t(E_F)$	4.44	4.52	4.98	5.68	4.28	4.14
γ	10.46	10.65	11.74	13.39	10.09	9.76

VI. ELASTIC CONSTANTS

The second-order elastic constants at equilibrium volumes and zero pressure are listed in Table VIII. Although C15 is not the stable ground state, we discuss the properties because the structure is very common for Laves phases and is closely related to that of C14, and it might appear at high temperatures.

To our knowledge, there are no experimental measurements on single-crystal elastic constants of $NbMn_2$. In Table VIII, the bulk moduli obtained from our work are close to those calculated by strain deformation, implying the precision of our calculations. Because the calculated equilibrium volume is smaller than the experimental one by 3%, the calculated elastic constants are expectedly larger by 10%, which is very common from calculations.

The results in Table VIII do not show any elastic instabilities [36] for the C14 and C15 phases of different magnetic orderings. In general, the values for the bulk moduli are about 250 GPa for the NM cases and about 200 to 220 GPa for the FM and AF cases. The smaller values for the magnetic cases are due to the slightly larger equilibrium volumes (Table I). Interestingly, in comparison to the calculated results of $ZrMn_2$, $TiMn_2$, and $NbCr_2$ the shear moduli c' of all compounds with C15 are almost the same. However, with the C14 structure, significant differences appear in different compounds. It is interesting to note that the C14 FM phase of $ZrMn_2$ has the lowest c_{66}, 18 GPa [12], whereas $NbMn_2$ and $TiMn_2$ have noticeably larger values, mainly due to weak magnetic interactions.

VII. VIBRATIONAL PROPERTIES

In order to study the temperature-dependent spin behaviors of $NbMn_2$, the vibrational spectra of the stablest C14 FM and C14 AF phases at their equilibrium volumes were calculated, with the intention being to overcome the inherent restriction to $T = 0$ K in standard DFT calculations of the electronic structure.

TABLE VIII. Calculated elastic constants (GPa), bulk moduli B (GPa), and linear combination shear modulus c' (GPa) at the optimized equilibrium volume for C15 and C14 phases of $NbMn_2$ compared to other Laves phases. The bulk moduli in parentheses are taken from the energy vs volume curves.

C15	c_{11}	c_{12}	c_{44}	B	c'		
$NbMn_2$ (NM)	316	215	96	249 (250)	50		
$NbMn_2$ (FM)	278	168	74	205 (206)	55		
$ZrMn_2$ (FM) [a]	250	150	21	184 (181)	50		
$TiMn_2$ (FM)	271	170	74	204 (203)	50		
$NbCr_2$ (NM) [b]	316	216	71	252	50		
C14	c_{11}	c_{12}	c_{13}	c_{33}	c_{44}	c_{66}	B
$NbMn_2$ (NM)	346	218	180	384	68	64	248 (248)
$NbMn_2$ (FM)	303	187	160	341	54	58	218 (220)
$NbMn_2$ (AF)	302	189	163	338	53	56	219 (219)
$ZrMn_2$ (FM) [a]	231	196	132	269	50	18	181 (180)
$TiMn_2$ (NM)	299	203	161	332	56	48	213 (209)

[a]Reference [12].
[b]Reference [35].

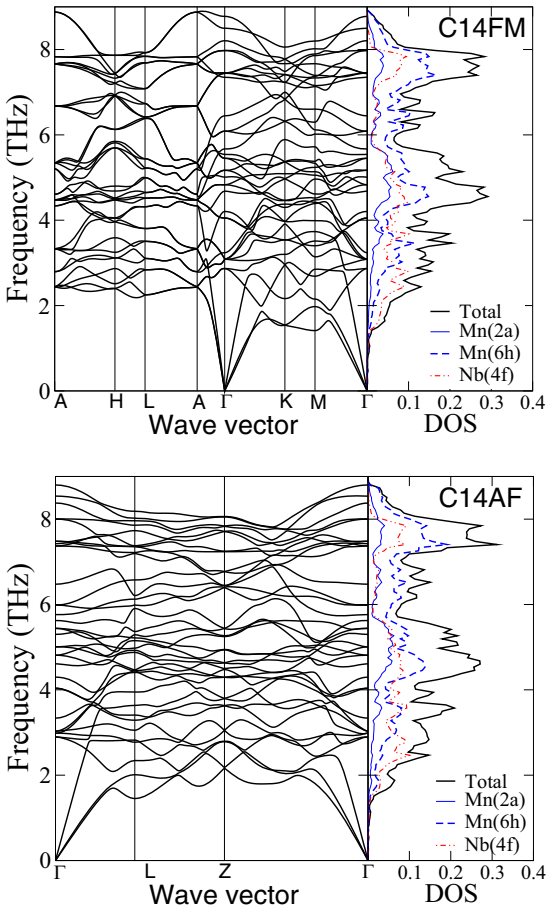

FIG. 7. DFT-derived phonon dispersions and DOSs for the C14 FM (top) and C14 AF (bottom) phases of $NbMn_2$.

Because the C14 AF phase of $NbMn_2$ is very close in DFT total energy to C14 FM, the vibrational properties are certainly of interest. Figure 7 shows the calculated phonon dispersions and the total and partial phonon densities of states (DOSs) for both phases. The total number of branches is 36 for the hexagonal C14 structure (12 atoms per unit cell). The phonon DOS of C14 AF is very similar to those of the C14 FM structure (left panel of Fig. 7). The main difference relevant at low temperatures appears at low frequencies, where vibrations of Mn($2a$) build up a weak peak at about 1.88 THz for C14 AF, which shifts to ~2.2 THz for C14 FM, mainly due to Mn($2a$) carrying no magnetic moments in the C14 AF phase.

For all phases studied, no modes with imaginary frequencies were found, indicating that they are dynamically stable.

The total free energy F within a DFT framework may be composed of two basic parts: the DFT ground-state total energy U_{DFT} for the electronic system at $T = 0$ K and the temperature-dependent free energy of the lattice vibrations. For the electronic part, the temperature dependence may be introduced by the model of Sommerfeld [37] based on the free-electron gas, involving the electronic DOS at Fermi energy. Within this model a temperature-dependent free energy for electrons F_{el} is derived. The vibrational free energy in the harmonic approximation is defined for finite temperatures once the phonon DOS is available [24]. Then, the total free energy

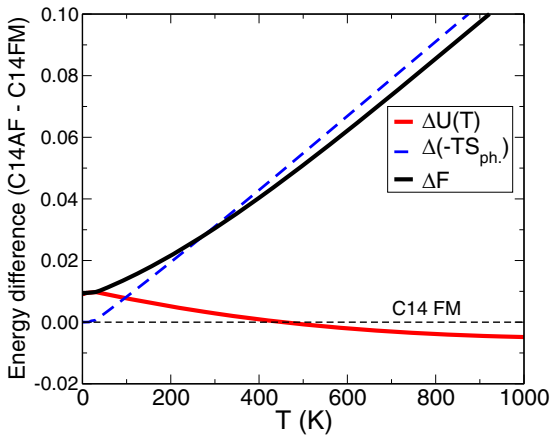

FIG. 8. Calculated temperature-dependent energy differences for $NbMn_2$: DFT-derived temperature-dependent total free-energy differences $\Delta F = F$(C14 AF) $-F$(C14 FM); internal energy differences $\Delta U(T) = U$(C14 AF) $- U$(C14 FM), including DFT total energies; and entropy differences $\Delta(-TS_{ph}) = (-TS_{ph.})$(C14 AF) $- (-TS_{ph})$(C14 FM). All energies are in kJ (mol f.u.)$^{-1}$. Positive values of ΔF are C14 FM stable; negative values are C14 AF stable. Thermodynamical properties calculated according to Ref. [24].

$F_{\rm ph}(T)$ is written as

$$F_{\rm ph}(T) = U_{\rm DFT}(0) + U_{\rm ph}(T) - TS_{\rm ph}(T), \qquad (6)$$

where the phonon free energy $F_{\rm ph}(T)$ is split into the internal energy $U_{\rm ph}(T)$ and entropy $TS_{\rm ph}(T)$. Equation (6) provides a reasonable approximation for the free energy at elevated temperatures as long as the harmonic approximation is valid. The temperature-dependent phase stabilities can then be derived by comparing the total free energies $F(T) = F_{\rm el} + F_{\rm ph}$ of different structures and magnetic orderings. Figure 8 shows the differences $\Delta F(T)$ of total free energies comparing the C14 AM and C14 FM phases.

The internal energy contains the zero-point energy $U_{ph}(0)$, which is similar for both phases (9.43 kJ/mol for C14 AF and 9.42 kJ/mol for C14 FM). The comparison of free energies of the C14 FM and C14 AF phases in Fig. 8 shows that C14 FM is slightly stable for all temperatures. Its stability increases with increasing temperature. At $T = 0$ K, the C14 FM phase degenerates. The most *striking* result is that the free-energy differences reach only 0.1 kJ (mol f.u.)$^{-1}$ up to 1000 K. This value is too small to identify a phase change experimentally to see which magnetic structure, C14 FM or C14 AF, is stable. At this elevated temperature anharmonic corrections could be of some influence, but deriving them from first principles is demanding and beyond the scope of this study. In particular, high accuracy would be needed because very small energy differences are involved. The temperature dependence of ΔF is driven by the phonon entropy difference $\Delta(-TS_{ph})$, as illustrated by Fig. 8. The electronic contribution is rather small. The differences in internal energies remain rather constant in the considered temperature range. Their weak dependence on temperature shows a trend opposite that of the entropy term. According to Fig. 8, the phonon entropies always favor the C14 FM phase with rather small free-energy differences.

VIII. CONCLUSION

According to the DFT results, the C14 FM and AF phases are nearly degenerate, and even at temperatures of several hundred kelvins the free-energy difference is only 0.02–0.03 kJ (mol f.u.)$^{-1}$. The FM phase is slightly favored over C14 AF. The magnetic phases, however, could not be confirmed so far experimentally. At very low temperatures, the free-energy difference between the two spin arrangements is less than 10^{-2} K, and therefore, spin flipping might be easily possible. Because some of the Mn atoms form a network of vertex-sharing tetrahedra in a kagome lattice as in cubic pyrochlore [1] (see Fig. 5), more complex arrangements of local Mn moments with rather degenerate free energies might be expected, increasing the degree of degeneracy and the residual entropy. This type of ground-state degeneracy of *antiferromagnetic* spin orderings might lead to a high electron density of states at the Fermi level, as is found in our results in Table VII and Fig. 6.

ACKNOWLEDGMENTS

Many thanks to Dr. A. Grytsiv for the quality confirmation of the single crystals and useful discussions. DFT calculations were done using the facilities of the Vienna Scientific Cluster.

[1] R. Moessner and A. P. Ramirez, Phys. Today **59**(2), 24 (2006).
[2] S. T. Bramwell and M. J. P. Gingras, Science **294**, 1495 (2001).
[3] A. P. Ramirez, A. Hayashi, R. J. Cava, R. Siddharthan, and B. S. Shastry, Nature (London) **399**, 333 (1999).
[4] S.-H. Lee, C. Broholm, W. Ratcliff, G. Gasparovic, Q. Huang, T. H. Kim, and S.-W. Cheong, Nature (London) **418**, 856 (2002).
[5] I. Mirebeau, I. N. Goncharenko, P. Cadavez-Peres, S. T. Bramwell, M. J. P. Gingras, and J. S. Gardner, Nature (London) **420**, 54 (2002).
[6] V. Fritsch, J. Hemberger, N. Büttgen, E.-W. Scheidt, H.-A. Krug von Nidda, A. Loidl, and V. Tsurkan, Phys. Rev. Lett. **92**, 116401 (2004).
[7] A. J. García-Adeva and D. L. Huber, Phys. Rev. Lett. **85**, 4598 (2000).
[8] E. Berg, E. Altman, and A. Auerbach, Phys. Rev. Lett. **90**, 147204 (2003).
[9] H. Nakamura, N. Metoki, S. Suzuki, F. Takayanagi, and M. Shiga, J. Phys. Condens. Matter **13**, 475 (2001).
[10] R. Ballou, E. Lelièvre-Berna, and B. Fåk, Phys. Rev. Lett. **76**, 2125 (1996).
[11] X.-Q. Chen, W. Wolf, R. Podloucky, P. Rogl, and M. Marsman, Europhys. Lett. **67**, 807 (2004).
[12] X.-Q. Chen, W. Wolf, R. Podloucky, P. Rogl, and M. Marsman, Phys. Rev. B **72**, 054440 (2005).
[13] M. Rotter, A. Grytsiv, X.-Q. Chen, P. Rogl, R. Podloucky, W. Wolf, V. T. Witusiewicz, A. Saccone, H. Noel, M. Doerr, A. Lindbaum, H. Michor, E. Bauer, S. Heathman, W. Kockelmann, and J. Taylor, Phys. Rev. B **74**, 224109 (2006).
[14] M. Brando, D. Moroni-Klementowicz, C. Albrecht, and F. Grosche, Phys. B (Amsterdam, Neth.) **378**, 111 (2006).
[15] M. Drys, J. Less. Common. Met. **75**, 261 (1980).

[16] V. Blavina and R. Trojko, J. Less. Common. Met. **119**, 297 (1986).
[17] G. Kresse and J. Furthmüller, Comput. Mater. Sci. **6**, 15 (1996).
[18] G. Kresse and J. Furthmüller, Phys. Rev. B **54**, 11169 (1996).
[19] P. E. Blöchl, Phys. Rev. B **50**, 17953 (1994).
[20] G. Kresse and D. Joubert, Phys. Rev. B **59**, 1758 (1999).
[21] J. P. Perdew and Y. Wang, Phys. Rev. B **45**, 13244 (1992).
[22] S. H. Vosko, L. Wilk, and M. Nusair, Can. J. Phys. **58**, 1200 (1980).
[23] X.-Q. Chen, R. Podloucky, and P. Rogl, J. Appl. Phys. **100**, 113901 (2006).
[24] X.-Q. Chen, W. Wolf, R. Podloucky, and P. Rogl, Phys. Rev. B **71**, 174101 (2005).
[25] K. Parlinski, Z. Q. Li, and Y. Kawazoe, Phys. Rev. Lett. **78**, 4063 (1997).
[26] X. Yan, X. Q. Chen, A. Grytsiv, V. T. Witusiewicz, P. Rogl, R. Podloucky, V. Pomjakushin, and G. Giester, Z. Metallkd. **97**, 450 (2006).
[27] X.-L. Yan, X.-Q. Chen, A. Grytsiv, P. Rogl, R. Podloucky, H. Schmidt, G. Giester, and X.-Y. Ding, Intermetallics **16**, 16 (2008).
[28] X. Chen, V. Witusiewicz, R. Podloucky, P. Rogl, and F. Sommer, Acta Mater. **51**, 1239 (2003).
[29] V. N. Svechnikov and V. V. Petkov, Metallofizika (Akad. Nauk Ukr. SSR, Inst. Metallofiz.) **64**, 24 (1976).
[30] T. Massalski, *Binary Alloy Phase Diagrams*, 2nd ed. (ASM International, Materials Park, OH, 1990), Vol. 3, p. 2578.
[31] V. Moruzzi, J. Janak, and A. Williams, *Calculated Electronic Properties of Metals* (Pergamon, New York, 1978), p. 164.
[32] E. Guggenheim, Trans. Faraday Soc. **33**, 151 (1937).
[33] A. Dinsdale, CALPHAD Comput. Coupling Phase Diagrams Thermochem. **15**, 317 (1991).
[34] X. Chen, W. Wolf, R. Podloucky, and P. Rogl, J. Alloy. Compd. **383**, 228 (2004).
[35] S. Hong and C. Fu, Intermetallics **7**, 5 (1999).
[36] J. F. Nye, *Physical Properties of Crystals: Their Representation by Tensors and Matrices* (Clarendon, Oxford, 1985), p. 142.
[37] W. Ashcroft and N. Mermin, *Solid State Physics* (Holt, Reinhart and Winston, New York, 1976), p. 47.